

On the Mesoscale Mechanism of Synthetic Calcium-Silicate-Hydrate Precipitation: A Population Balance Modeling Approach

M. Reza Andalibi,^{†,‡,} Abhishek Kumar,^{‡,§} Bhuvanesh Srinivasan,[‡] Paul Bowen,[‡] Karen*

Scrivener,[§] Christian Ludwig^{†,‡}, Andrea Testino[†]

[†] Energy and Environment Research Department, Paul Scherrer Institute (PSI), Villigen-PSI, Switzerland

[‡] Materials Institute, Powder Technology Laboratory (LTP), EPFL, Lausanne, Switzerland

[§] Laboratory of Construction Materials EPFL, Lausanne, Switzerland

[‡] ENAC-IIIE, EPFL, Lausanne, Switzerland

* Corresponding author: reza.andalibi@psi.ch

Electronic Supplementary Information

S1.	Experimental details	S2
S2.	Fundamentals of population balance equation	S2
S3.	Aqueous speciation and thermodynamic driving force for solid formation	S7
S4.	Crystallite/particle size and parameters for secondary nucleation	S11
S5.	Coupled thermodynamic-kinetic modeling framework	S14
S6.	Regression of the computational model to experimental data	S15
S7.	Some supplementary outputs of PBEM	S17
S8.	Mechanistic growth rate equations	S19
S9.	Additional supplementary Fig.s	S25
S10.	References	S28

S1. Experimental details

C-S-H precipitation kinetic data were collected using a home-made laboratory-scale reactor working in a semibatch manner, the details of which are described elsewhere.¹ The system was operated at 298.15 K and atmospheric pressure under nitrogen to avoid carbonation. With the aim of producing C-S-H of Ca:Si = 2 as the final precipitate, 22 mL of a 1 M aqueous NaOH solution was mixed with 200 mL of a 0.01 M Na₂SiO₃·5H₂O solution and the mixture was added in a dropwise manner to a premixed 200 mL solution of 0.02 M Ca(NO₃)₂·4H₂O (Fig. S1). Kinetic data were collected for two different flow rates of the silicate + NaOH stream ($Q = 2.00$ and $0.50 \text{ mL}\cdot\text{min}^{-1}$). Further details on the characterization, as well as atomistic structure from NMR measurements and atomistic modeling of this C-S-H can be found in an earlier work by Kumar et al.¹

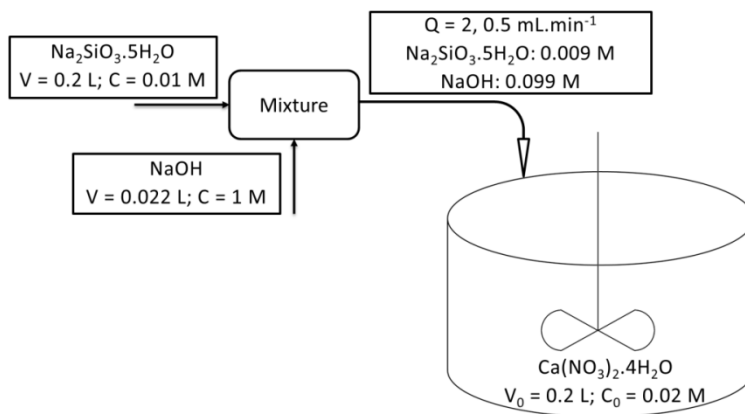


Fig. S1. Schematic representation of semi-batch reactor used for experimental data collection.

S2. Fundamentals of population balance equation

In this section we present a brief overview on population balance equation and its solution using Quadrature Method of Moments (QMOM). For a detailed introduction to PBE, the reader is referred to the seminal work of Hulburt and Katz,² and that by Randolph and Larson.³ For an exhaustive primer on various quadrature-based methods the text by Marchisio and Fox is an excellent reference.⁴

Consider a system containing particulate material. In such a system, a particle can be represented by two sets of coordinates denoted as external and internal coordinates. External coordinates represent

the spatial position of the particle in the physical space, $\mathbf{x} \equiv (x_1, x_2, x_3)$. On the other hand, internal coordinates describe some intrinsic properties of the population, e.g., particle size, particle velocity, temperature, composition, etc. To quantitatively describe the variations in the population of particles across the external and internal spaces one may resort to the so-called number-density function (NDF). Consider a population of dispersed entities in an infinitesimal control volume $d\mathbf{x} \equiv dx_1 dx_2 dx_3$ centered at the physical point \mathbf{x} in the external space. Let $\mathbf{L} \equiv (L_1, L_2, \dots, L_M)$ be the internal coordinate vector containing the respective M internal coordinates. The NDF $n(t, \mathbf{x}, \mathbf{L})$ is defined as the number of particles in the infinitesimal physical volume $d\mathbf{x}$ and infinitesimal phase space volume $d\mathbf{L}$. The NDF is therefore a function of time (t), space (\mathbf{x}), and the internal coordinate vector (\mathbf{L}) and may be further normalized by the total physical volume of the system being considered. It is worth noting the NDF is an average quantity representative of particle populations in infinitesimal control volumes with differential dimensions in both internal and external spaces.⁴ Hereafter, we concentrate on population distributions which are homogeneous across the external space, and only track particle size as an internal coordinate (univariate PBE). Here, homogeneity assumption is justified as we are working with a well-mixed, relatively small lab-scale reactor. Hence, NDF would merely be a function of time and particle size, $n(t, L)$.

The second important definition is that of k^{th} order moment of the density function

$$m_k \equiv \int_{\Omega_L} L^k n(t, L) dL \quad (\text{S1})$$

where Ω_L is the particle size domain (theoretically $0-\infty$). As it can be readily understood from equation (1), for univariate size-based NDF the zeroth and first moments represent the total particle number and total particle length per unit volume of the system, respectively. Moreover, the second and third moments are proportional to the total particle surface area and total particle volume per unit system volume, respectively. In the two latter cases, the proportionality constants are area and volume shape factors (k_A and k_V , respectively). One can further convert particle volume to particle mass using the

particle density (ρ_{solid}). Number-averaged values can be easily obtained through dividing the respective moment by the zeroth moment.³ Furthermore, an average particle size can be defined by m_{k+1}/m_k for any value of k (e.g., for Sauter mean diameter $k = 2$).⁴ Other useful definitions can be found in general texts.^{3,4}

For a homogeneous system (uniform NDF across the physical space) the general population balance equation describing the variation of NDF over time and phase space can be written as³

$$\frac{\partial n}{\partial t} + \frac{\partial}{\partial L}(nG_L) + n \frac{d(\ln V)}{dt} = - \sum_{j=1}^F \frac{Q_j n_j}{V} + h \quad (\text{S2})$$

where G_L is the rate of change of particle size ($\frac{dL}{dt}$; linear growth rate), V is the system volume, F is the number of input and output flows (taken as positive for flow out of the suspension and negative for flow into the suspension), and h represents discontinuous jumps signifying discrete events (e.g., nucleation, aggregation, or breakage).⁴ Now let us multiply both sides of equation (2) by L^k and integrate from zero to infinity. After simplification

$$\frac{dm_k}{dt} + m_k \frac{d(\ln V)}{dt} = k \int_0^\infty n(t, L) G_L L^{k-1} dL - \sum_{j=1}^F \frac{Q_j m_{k,j}}{V} + \bar{h}_k \quad (\text{S3})$$

where $m_{k,j}$ is the k^{th} moment in the j^{th} flow and \bar{h}_k is

$$\bar{h}_k = \int_0^\infty h L^k dL \quad (\text{S4})$$

In order to solve equation (3) for a particulate system, the set of equations for the first k moments of interest should be closed, i.e., involve only functions of the moments themselves, which is in most cases not the case (for example, with size-dependent growth rate, the integral on the right-hand side of equation (3) cannot be directly evaluated).^{5,6} Since moments depend on time, the moment closure problem has to be solved at every time step during numerical integration of differential equations. Therefore, the numerical algorithm for its solution has to be efficient and fast. For this purpose

quadrature-based moment methods that reconstruct the NDF from a finite set of moments will be employed.⁴

In univariate QMOM the closure problem (i.e., calculating integrals dependent on $n(t,L)$) is overcome by resorting to an interpolation formula

$$\int_{\Omega_L} n(t,L)g(L)dL \approx \sum_{\alpha=1}^N w_{\alpha}g(L_{\alpha}) \quad (S5)$$

where $g(L)$ is any function of interest while w_{α} and L_{α} are, respectively, the weights and nodes of the interpolation formula, and N is the number of nodes used to approximate the NDF (quadrature order). Unit consistency dictates that w_{α} have units equivalent to $n(t,L)dL$ (# particles. m^{-3} suspension). QMOM takes advantage of Gaussian quadrature of order N which offers a degree of accuracy of $2N$. Therefore, it will be able to capture the first $2N$ moments of the weight function. Conversely, N nodes (abscissas) and N weights shall be obtained by solving the following nonlinear system, assuming the knowledge of the first $2N$ moments of NDF

$$\begin{aligned} m_0 &= \sum_{\alpha=1}^N w_{\alpha} \\ m_1 &= \sum_{\alpha=1}^N w_{\alpha}L_{\alpha} \\ &\dots \\ m_{2N-1} &= \sum_{\alpha=1}^N w_{\alpha}L_{\alpha}^{2N-1} \end{aligned} \quad (S6)$$

Since the above system requires a very good initial guess in order to ensure convergence, one may take advantage of the orthogonal polynomials theorem. According to this theory, a Gaussian quadrature is an interpolation formula whose N nodes are the roots of polynomial $P_N(L)$ orthogonal to the weight function $n(L)$.⁷ Among the algorithms available in order to calculate the weights and abscissas from the knowledge of a moment set, the product-difference (PD) algorithm of Gordon⁸ and the Wheeler

algorithm^{9,10} are useful for an arbitrary NDF. However, the latter is more stable, and is able to handle distributions with zero mean ($m_1 = 0$).⁴ Fig. S2 schematically shows the application of Wheeler algorithm in order to approximate a normal distribution using 3, 4, and 5 quadrature nodes.

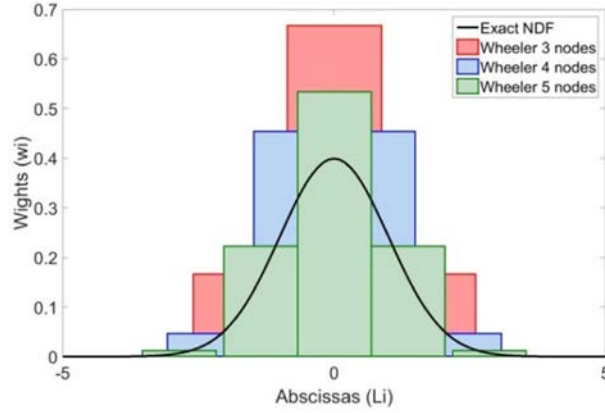


Fig. S2. Quadrature approximation of a normal distribution using Wheeler algorithm.

In this study, we have implemented primary nucleation, true secondary nucleation, and molecular growth as the subprocesses that govern the overall precipitation reaction. Inserting primary and secondary nucleation rates into equation 4,

$$\bar{h}_k = (L_I)^k \times J_I(t) + (L_{II})^k \times J_{II}(t) \quad (S7)$$

where J_I and J_{II} are primary and secondary nucleation rates (# crystallites. $m^{-3}.s^{-1}$), and finally, L_I and L_{II} are the corresponding critical size of nuclei (m). Also using equation 5

$$k \int_0^\infty n(t, L) G_L L^{k-1} dL \approx k \sum_{\alpha=1}^N w_\alpha(t) G(L_\alpha(t)) (L_\alpha(t))^{k-1}; k = 0, 1, \dots, 2N - 1 \quad (S8)$$

For our semi-batch reaction scheme with constant inlet flow rate and no particle inflow, combining equations S3, S7, S8 gives the final form of PBE set to be solved (equation 1 in the main text; the only flow rate, coming into the reactor, is denoted by Q). Note that working with dilute solutions (ionic strength < 0.08 mol.kg⁻¹ solvent) the volume change on mixing is negligible as also confirmed by calculations in OLI Studio.¹¹

S3. Aqueous speciation and thermodynamic driving force for solid formation

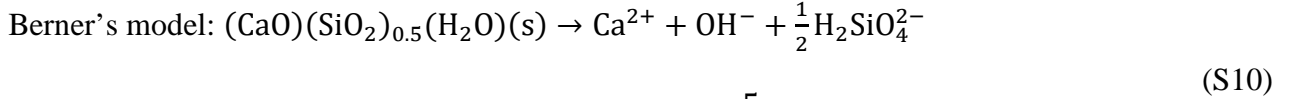
Among the solid solution models available for C-S-H solid phase those proposed by Berner,^{12,13} Kersten,¹⁴ and Carey and Lichtner¹⁵ allow for the formation of a homogeneous phase with Ca:Si = 2 (the composition of interest to us). Other models cannot describe such a solid composition (at least as a single homogeneous phase) and they attempt to model the solid solution—aqueous solution equilibrium by forcing portlandite equilibrium beyond some Ca:Si ratio which is always less than 2 (e.g., > 1.5 in the model of Rahman et al.¹⁶ and > 1.5-1.9 in the model of Kulik and Kersten¹⁷).¹⁸ The former is in contrast to our observation of uniform C-S-H (Ca:Si = 2) precipitation without any portlandite forming from solution.¹ Our C-S-H phase corresponds to 1:1 solid solution of Ca(OH)₂ and CaH₂SiO₄ end-members in Berner's model,¹² 1:1 solid solution of Ca(OH)₂ and CaHSiO_{3.5}·1.5H₂O end-members in Kersten's model,¹⁴ and 1:2 solid solution of SiO₂·2H₂O and Ca(OH)₂ end-members in Carey and Lichtner's model.¹⁵

As Prieto discussed, for practical purposes the so-called stoichiometric *solubility* product shall be used to describe the dissolution/precipitation behavior of solid solutions. In reality the former represents a metastable equilibrium condition which assumes the solid solution to be a stoichiometric phase (i.e., a pure single-component solid with fixed stoichiometry) dissolving/precipitating in a congruent manner. This concept arises from experimental observations that solid solutions tend to dissolve in a congruent manner until an initial saturation is built up. Nevertheless, an aqueous solution may remain in metastable state of saturation with respect to stoichiometric solid because reaching the true equilibrium necessitates dissolution-reprecipitation of the solid solution, which can be an extremely sluggish process.^{19,20} Indeed, according to Berner such a simplifying assumption is reasonable for C-S-H precipitation at room temperature within the time scales of experimental setups.¹² Having the former in mind and in line with many studies in the literature that use the concept of stoichiometric solubility product in explaining the precipitation of solid solutions,²¹⁻²⁶ we will apply the same framework to define the thermodynamic driving force for C-S-H precipitation. By definition, the stoichiometric

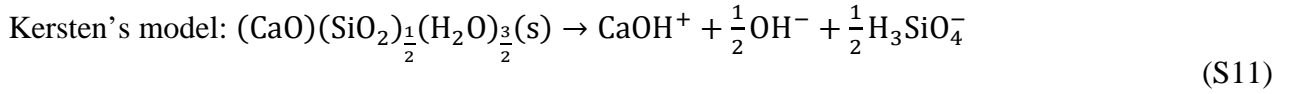
solubility product (superscript ‘st’) for a binary solid solution with end-member solubility constants K_1 and K_2 reads

$$K_{sp}^{st} = (K_1 X_1 \lambda_1)^{X_1} (K_2 X_2 \lambda_2)^{X_2} \quad (S9)$$

where X_1 and $X_2 = 1 - X_1$ are mole fractions of end-members composing one mole of solid solution, and λ_1 and λ_2 are their activity coefficients, respectively. Writing the dissolution reaction for our particular C-S-H phase according to the three selected models described earlier

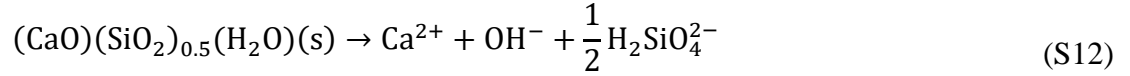


$$K_{sp}^{Berner} = 9.99 \times 10^{-8}; v_{Berner} = \frac{5}{2}$$



$$K_{sp}^{Kersten} = 3.54 \times 10^{-7}; v_{Kersten} = 2$$

Carey and Lichtner’s model:



$$K_{sp}^{CL} = 5.89 \times 10^{-7}; v_{CL} = \frac{7}{3}$$

where v is the total number of ions produced by one of formula unit of solid upon dissolution. Knowing the solubility product, the (molal) activities of aqueous species (Ca^{2+} , OH^- , and $H_2SiO_4^{2-}$ for the model of Berner; $CaOH^+$, OH^- , and $H_3SiO_4^-$ for the model of Kersten; and Ca^{2+} , OH^- , and H_4SiO_4 for the model of Carey and Lichtner) are needed for the calculation of ionic activity products (IAP)^{27,28}

$$IAP^{Berner} = a_{Ca^{2+}} \times a_{OH^-} \times a_{H_2SiO_4^{2-}}^{\frac{1}{2}} \quad (S13)$$

$$IAP^{Kersten} = a_{CaOH^+} \times a_{OH^-}^{\frac{1}{2}} \times a_{H_3SiO_4^-}^{\frac{1}{2}} \quad (S14)$$

$$IAP^{CL} = a_{Ca^{2+}}^{\frac{2}{3}} \times a_{OH^-}^{\frac{4}{3}} \times a_{H_4SiO_4}^{\frac{1}{3}} \quad (S15)$$

with a denoting molal activities of different aqueous species. Subsequently, the supersaturation ratio is defined as²⁹

$$S^{\text{modelX}} = \left(\frac{\text{IAP}^{\text{modelX}}}{K_{\text{sp}}^{\text{modelX}}} \right)^{1/\nu_{\text{modelX}}} \quad (\text{S16})$$

with modelX denoting respective C-S-H models. In order to calculate the molal activities used in IAP expressions (equations (13-15)), consistent with the general practice used in modeling precipitation processes, we assume that upon any perturbation (i.e., overall change of elemental balance) the aqueous species attain equilibrium state quickly compared to the time-scale of solid formation process.³⁰⁻³⁶ In this manner, the system is assumed to always experience a locally-equilibrated state where aqueous species attain their equilibrium distribution quickly before they contribute to the formation of solid phase, the latter being the rate limiting step.^{31,37} This view necessitates the calculation of speciation in the aqueous phase during the period of kinetic process.

One further step in the selection of a suitable C-S-H model was to compare the mole amount of Ca^{2+} in solution after the system has reached equilibrium. Among the experiments conducted, at flow rate $2 \text{ mL}\cdot\text{min}^{-1}$ equilibrium was reached after a reasonable period of time (~ 1 day). Comparison between the experimentally measured equilibrium Ca^{2+} mole amount and that predicted using different C-S-H models revealed that Kersten's model reproduces the experimental data better than the other two models. However, some adjustment in the value of $\text{p}K_{\text{sp}}$ (0.77 pK units) rendered the C-S-H model completely consistent with the experimental data. The preceding adjustment is justified in the light of the relatively large scatter in experimental C-S-H solubility data used to fit solid solution models.³⁸ Therefore, a value of $K_{\text{sp}}^{\text{Kersten,adjusted}} = 6.0313 \times 10^{-8}$ was used in all the simulations.

An equilibrium speciation solver to be coupled into a kinetic simulation code must be accurate and efficient.³⁹ In order to avoid computationally expensive communication with external speciation solvers we chose to develop our own equilibrium solver based on the algorithm proposed by Anderson and Crerar adapted to our needs (*c.f.*, Zhu et al.³⁵ for an example of interfacing OLI Studio with population

balance modeling).^{40,41} The Truesdell-Jones (TJ) activity coefficient parameters and also mass action equations (with their corresponding equilibrium constant) provided to the speciation solver are summarized in Table S1 and Table S2. Throughout this work, equilibrium calculations considering the formation of solid C-S-H are denoted as EQBRM while those merely considering aqueous reactions (local equilibrium in aqueous solution) are denoted as aqEQBRM.

Table S1. Aqueous species considered here along with their TJ activity coefficient parameters (taken from PHREEQC database⁴² whenever available or estimated by fitting TJ model to activity data calculated by OLI

Studio¹¹ over an ionic strength < 1 mol.kg⁻¹).

Species name	Truesdell-Jones Parameters	
	a _i	b _i
H ₂ O	0	0
Ca ²⁺	4.86	0.15
H ₃ SiO ₄ ⁻	4.5	0.06
Na ⁺	4.32	0.06
NO ₃ ⁻	3.58	0
OH ⁻	10.65	0.21
H ⁺	4.78	0.24
NaNO ₃	0	0.08
CaNO ₃ ⁺	3.93	0.06
H ₄ SiO ₄	0	0.05
H ₂ SiO ₄ ²⁻	3.74	0
CaOH ⁺	3.95	0.06
CaHSiO ₃ ⁺	3.22	0.01
CaH ₂ SiO ₄	0	0.05
NaHSiO ₃	0	0.05

Table S2. Mass action equations for model C-S-H precipitation system and their equilibrium constants at T = 298.15**K (from OLI Studio database).¹¹**

Index	Law of mass action	$\log_{10}(K_i)$
1	$H^+ + OH^- \rightleftharpoons H_2O$	13.99340
2	$H_3SiO_4^- + H^+ \rightleftharpoons H_4SiO_4$	9.84214
3	$H_2SiO_4^{2-} + H^+ \rightleftharpoons H_3SiO_4^-$	13.10291
4	$Na^+ + H_3SiO_4^- \rightleftharpoons NaHSiO_3 + H_2O$	2.08340
5	$NaNO_3 \rightleftharpoons Na^+ + NO_3^-$	0.91046
6	$CaOH^+ \rightleftharpoons Ca^{2+} + OH^-$	-1.23140
7	$CaNO_3^+ \rightleftharpoons Ca^{2+} + NO_3^-$	-0.41911
8	$Ca^{2+} + H_3SiO_4^- \rightleftharpoons CaHSiO_3^+ + H_2O$	1.25827
9	$CaH_2SiO_4 + H^+ \rightleftharpoons Ca^{2+} + H_3SiO_4^-$	8.35399

S4. Crystallite/particle size and parameters for secondary nucleation

In the absence of preformed solid particles, nucleation would be the first step in the precipitation of a solid phase from a liquid solution. Broadly speaking, nucleation is classified as either primary or secondary nucleation. In contrast to primary nucleation, secondary nucleation takes place merely in the presence of already formed precipitant particles (either formed earlier during the same precipitation process or added to the reaction medium, for instance as seeds). Primary nucleation could be either homogeneous or heterogeneous which, respectively, proceed in the absence or presence of foreign surfaces. The theoretical frameworks for the two primary nucleation mechanisms are similar, differing mainly in the magnitude of interfacial tension used in their mathematical description.⁴³ Regarding secondary nucleation in the presence of solid precipitate, it is important to distinguish between apparent, contact and true (catalytic) mechanisms.^{29,44} Apparent mechanisms refer to those taking place when nuclei are introduced into the system along with seeding crystals. On the other hand, contact

mechanisms, which give rise to nuclei as a result of mechanical contact between crystals and crystallizer components or crystals themselves, generally occur for particles larger than 0.2-0.5 μm . Finally, true (catalytic) secondary nucleation is a prevalent process in the formation of polycrystalline/mesocrystalline particles, once we have precipitated particles in solution.⁴⁵⁻⁴⁹ Indeed, catalytic secondary nucleation allows for the formation of nuclei at lower supersaturation ratios due to the favorable interaction between existing embryos and already precipitated particles.^{43,44,46,50-52} This lower energy demand due to nucleation in the close vicinity of already formed substrate can be accounted for as follows.

If we assume that C-S-H crystallites are cuboids of arbitrary aspect ratio (Fig. 2 (c) in the main text) their surface area and volume would be

$$A_c \equiv k_A L_c^2 = 2a_r(a_r + 2)L_c^2 \quad (\text{S17})$$

$$V_c \equiv k_V L_c^3 = a_r^2 L_c^3 \quad (\text{S18})$$

Therefore, we will have surface area and volume shape factors $k_A = 2a_r(a_r + 2)$ and $k_V = a_r^2$, respectively, which are dependent on the ratio of crystallite edge length to its thickness (Fig. 2 (c)). When a cuboidal secondary nuclei forms in the close vicinity of the peripheral area of a substrate, one out of its four side faces interacts with the substrate surface while the rest of them are in contact with bulk solution (look at Fig. 1 and Fig. 2 (b) in the main text). The former face experiences stabilization due to attractive interaction with the substrate. If we take σ ($\text{J}\cdot\text{m}^{-2}$) to be the adhesion/cohesion energy between these two surfaces per unit, then the work required in order to form a new surface as a secondary nucleus (the interfacial term in classical nucleation theory) would be

$$2a_r(a_r + 2)L_c^2 \times \gamma_{\text{eff}} \equiv (3a_r + 2a_r^2)L_c^2 \times \gamma + a_r L_c^2 \times (\gamma - \sigma) \quad (\text{S19})$$

After some algebraic manipulation and simplification we arrive at equation 7 in the main text, which reduces to the equation derived for cubes by Testino et al. in case of $a_r = 1$.⁴⁶

Now let us estimate the fraction of overall surface area that is available for secondary nucleation. To account for the foil-like morphology of C-S-H particles,¹ we assume that secondary nucleation

occurs only laterally on the peripheral area of already formed C-S-H particles. Therefore, at each instant of time, out of the overall crystallite surface area, which is proportional to the second moment (Section S2), only the side particle surfaces are available for secondary nucleation. PBEM tracks L_c as a function of time and average particle edge length (L_p) is estimated at each time step knowing the overall volume of solid precipitated out of solution. In this respect, the average crystallite thickness (\bar{L}_c) shall be defined as³

$$\bar{L}_c(t) = \sqrt[3]{\frac{m_3(t)}{m_0(t)}} \quad (\text{S20})$$

Alternatively, the total number of crystallites at time t ($n_c(t)$) reads

$$n_c(t) = m_0(t) \times V(t) = \int_{\tau=0}^{\tau=t} (J_I(\tau) + J_{II}(\tau))V(\tau)d\tau \quad (\text{S21})$$

Thus, equation 20 can also be written as

$$\bar{L}_c(t) = \sqrt[3]{\frac{m_3(t) \times V(t)}{n_c(t)}} \quad (\text{S22})$$

In order to form particles, *individual* primary nuclei are needed around which secondary nuclei can be generated. For that reason, each particle is made up of a single primary nucleation-generated nucleus and possibly several secondary nucleation-generated nuclei. Bearing that in mind, the total number of particles at time t ($n_p(t)$) is

$$n_p(t) = \int_{\tau=0}^{\tau=t} J_I(\tau) \times V(\tau)d\tau \quad (\text{S23})$$

Now, the overall precipitate volume ($V_{\text{CSH}}(t)$) can be estimated from the third moment (or equivalently from the n_c and \bar{L}_c)

$$V_{\text{CSH}}(t) = k_V m_3(t) \times V(t) = n_c(t) \times k_V (\bar{L}_c(t))^3 \quad (\text{S24})$$

As we assumed a lateral or edge secondary nucleation, which necessitates particles of thickness \bar{L}_c , the volume equivalent mean edge length of particles would be (Fig. 2 (b))

$$\bar{L}_p(t) = \bar{L}_c(t) \times \sqrt{\frac{k_v n_c(t)}{n_p(t)}} \quad (\text{S25})$$

From Fig. 1 and Fig. 2 (b) it is clear that only the external side faces of particles are available for secondary nucleation. Hence, the fraction of overall precipitate surface area available for secondary nucleation would be

$$x_A(t) = \frac{4\bar{L}_c(t) \times \bar{L}_p(t) \times n_p(t)}{k_A m_2(t) \times V(t)} \quad (\text{S26})$$

S5. Coupled thermodynamic-kinetic modeling framework

The set of moment-transformed PBE (equation (1) in the main text) has to be solved simultaneously with mass balance equations. These mass balance equations track the time evolution of elemental abundances in aqueous solution that is passed at every times-step into the speciation solver. For the current C-S-H precipitation system, there are four elemental balance equations that have to be considered (O, Ca, Si, and Na; the overall amount of nitrogen in solution is constant as no N-containing compound is being introduced into the aqueous solution nor leaving it (Fig. S1):

$$\frac{d}{dt} n_{O,Sol} = Q_1 C_O - v_O \frac{dn_{C-S-H}}{dt} \quad (\text{S27})$$

$$\frac{d}{dt} n_{Ca,Sol} = -v_{Ca} \frac{dn_{C-S-H}}{dt} \quad (\text{S28})$$

$$\frac{d}{dt} n_{Si,Sol} = Q_1 C_{Si} - v_{Si} \frac{dn_{C-S-H}}{dt} \quad (\text{S29})$$

$$\frac{d}{dt} n_{Na,Sol} = Q_1 C_{Na} \quad (\text{S30})$$

where $n_{X,Sol}$ denotes the molar amount of element X in solution having a molar concentration C_X (mol.m^{-3}) in the inlet stream of flow rate $Q_1(\text{m}^3)$, and contributing v_X moles in one mole C-S-H precipitated from solution. Additionally,

$$\frac{dn_{\text{C-S-H}}}{dt} = k_V \rho_{\text{solid}} V(t) \times \left(3 \sum_{i=1}^N w_i(t) G(L_i(t)) (L_i(t))^2 + (L_I)^3 \times J_I(t) + (L_{II})^3 \times J_{II}(t) \right) \quad (\text{S31})$$

is the overall rate of C-S-H precipitation due to nucleation (second and third terms) and growth (first term) events (mol.s^{-1}). This equation is nothing but the ODE for the third moment (equation 1 in the main text with $k = 3$) multiplied by some factors to convert it into the rate of C-S-H precipitation in mol.s^{-1} . As per system specifications, C_O , C_{Si} , and C_{Na} are 55.48, 0.009, and 0.1172 mol.L^{-1} , respectively (Fig. S1). Also, according to Kersten's C-S-H model, ν_O , ν_{Ca} , ν_{Si} are 7/2, 1, and 1/2, respectively.

S6. Regression of the computational model to experimental data

Having no unknown model parameters, solution of the PBE set (equation (1) in the main text), written for three quadrature nodes, coupled to mass balance equations give temporal evolution of different elements in solution as well as solid C-S-H formed. Additionally, at each time step of integrating the ODE set the speciation solver calculates the full speciation of aqueous solution. Nevertheless, the former is rarely the case and we oftentimes have at least a few unknown model parameters that have to be estimated by fitting the computational model into some experimental dataset. In this work, we have five unknown parameters to be optimized: γ , σ , k_r , g , a_r . The objective function to be minimized is defined as

$$F_{\text{objective}} = 10^6 \times \sum (n_{\text{Ca,experiment}} - n_{\text{Ca,simulated}})^2 \quad (\text{S32})$$

where $n_{\text{Ca,experiment}}$ and $n_{\text{Ca,simulated}}$ are the experimental and corresponding simulated $\text{Ca}^{2+}(\text{aq})$ mole amounts, respectively, and 10^6 is a scaling factor to bring the objective function to an order of magnitude of one.⁵³ A bounded Nelder-Mead simplex direct search code, which uses MATLAB's

fminsearch function as the engine, was employed to minimize the objective function.⁵⁴ All the codes, included in Supplementary Information, were implemented in MATLAB® 2015b.

The time-dependent experimental data ($\text{Ca}^{2+}(\text{aq})$ mole amount as a function of time) already collected on the precipitation of C-S-H will be used in order to examine the kinetics of this model system. The overall regression algorithm is summarized schematically in Fig. 3 in the main text. As can be seen the first step would be to introduce the experimental data into the model along with initial conditions for all the ordinary differential equations (ODEs). Furthermore, appropriate initial guesses should be provided for unknown model parameters. Having the initial amounts of various elements (e.g., Ca and Si), an initial speciation calculation shall be done to determine the concentrations of various aqueous species in the solution assuming equilibrium is attained quickly in the liquid phase while the subsequent precipitation process would be the rate limiting step (local-equilibrium assumption).³²⁻³⁵ Knowing the aqueous speciation one may calculate the driving force for the formation of new solid phase, the supersaturation ratio, by comparing the ion activity product (IAP) of relevant species with their corresponding equilibrium value (K_{sp}).²⁷ Having the supersaturation ratio, kinetic equations describing different particle formation processes (e.g., nucleation and growth) can be used to calculate various terms in the PBE set which is marched over time along with mass balances and changes in the system volume. After each time step in the integration of the ODE set, speciation should be calculated using the updated amounts of elements. Further, recently calculated moments are introduced into the Wheeler algorithm to calculate the corresponding quadrature nodes and weights necessary for some integral terms in PBE set. The former along with the updated supersaturation ratio are used to advance the ODE set one more time step. This (internal) loop is iterated over until we reach the end of simulation period (literally the period for which experimental data is regressed). At this step, an external loop (optimization scheme) constructs an objective function using the summed squared differences between the experimental data and equivalent simulated values. The unknown model parameters are adjusted in response to objective function values larger than a pre-defined tolerance and

passed to the internal loop for a new coupled thermodynamic-kinetic simulation. Iteration over the external loop will finally give the optimal model parameters describing the experimental data most accurately.

In this work, all the simulations were run on an ordinary HP laptop with dual-core Intel® Core™ i5-4310M CPU @ 2.70 GHz 2.70 GHz processor and 8.00 GB of RAM. A typical run time of ~ 150 seconds was required for a 24 hour precipitation simulation with known model parameters. To keep the optimization runs in a feasible range (a few hours), however, only the experimental data down to 99.0 % conversion were used for the model regressions. This corresponds to 670 and 330 minutes for $Q = 0.5$ and $2.0 \text{ mL}\cdot\text{min}^{-1}$ datasets, respectively (Fig. 4 in the main text). For the sake of completeness, the experimental data collected over 24 h along with corresponding simulation results are presented as insets.

S7. Some supplementary outputs of PBEM

From the results of PBE simulation it is possible to estimate the average supersaturation ratio at which each of the constituting events occurs:

$$\overline{S}_{J_I} = \frac{\int_{\tau=0}^{\tau=t} S \times V(\tau) J_I(\tau) (L_I(\tau))^3 d\tau}{\int_{\tau=0}^{\tau=t} V(\tau) J_I(\tau) (L_I(\tau))^3 d\tau} \quad (\text{S33})$$

$$\overline{S}_{J_{II}} = \frac{\int_{\tau=0}^{\tau=t} S \times V(\tau) J_{II}(\tau) (L_{II}(\tau))^3 d\tau}{\int_{\tau=0}^{\tau=t} V(\tau) J_{II}(\tau) (L_{II}(\tau))^3 d\tau} \quad (\text{S34})$$

$$\overline{S}_G = \frac{\int_{\tau=0}^{\tau=t} S \times V(\tau) \times \left[\frac{dm_3}{d\tau} - J_I(\tau) (L_I(\tau))^3 - J_{II}(\tau) (L_{II}(\tau))^3 \right] d\tau}{\int_{\tau=0}^{\tau=t} V(\tau) \times \left[\frac{dm_3}{d\tau} - J_I(\tau) (L_I(\tau))^3 - J_{II}(\tau) (L_{II}(\tau))^3 \right] d\tau} \quad (\text{S35})$$

where \overline{S}_{J_I} , $\overline{S}_{J_{II}}$, and \overline{S}_G denote volume-averaged supersaturation ratios for primary nucleation, secondary nucleation, and growth, respectively. Table S3 compiles the activation free energies for the nucleation events along with the range of their critical nuclei size, and also the average supersaturation ratios over which each of the nucleation and growth events takes place.

Another quantity that can be estimated from PBE simulations is the contribution of individual events to the overall precipitation process:

$$n_{\text{CSH}}^{\text{JI}} = 100 \times \frac{\int_{\tau=0}^{\tau=t} V(\tau) J_{\text{I}}(\tau) (L_{\text{I}}(\tau))^3 d\tau}{\int_{\tau=0}^{\tau=t} V(\tau) m_3(\tau) d\tau} \quad (\text{S36})$$

$$n_{\text{CSH}}^{\text{JII}} = 100 \times \frac{\int_{\tau=0}^{\tau=t} V(\tau) J_{\text{II}}(\tau) (L_{\text{II}}(\tau))^3 d\tau}{\int_{\tau=0}^{\tau=t} V(\tau) m_3(\tau) d\tau} \quad (\text{S37})$$

$$n_{\text{CSH}}^{\text{G}} = 100 - (n_{\text{CSH}}^{\text{JI}} + n_{\text{CSH}}^{\text{JII}}) \quad (\text{S38})$$

with $n_{\text{CSH}}^{\text{JI}}$, $n_{\text{CSH}}^{\text{JII}}$, and $n_{\text{CSH}}^{\text{G}}$ representing cumulative amounts of C-S-H precipitated (in percentage of the overall solid formed) as a result of primary nucleation, secondary nucleation, and growth, respectively.

Table S3. Critical size of nuclei along with activation free energies and average supersaturation ratios of various events estimated from PBEM.

Q (mL.min ⁻¹)	L _I (nm) ¹	L _{II} (nm) ¹	$\Delta G_{\text{max,I}}$ (kJ.mol ⁻¹) ^a	$\Delta G_{\text{max,II}}$ (kJ.mol ⁻¹) ^a	\bar{S}_{JI}	\bar{S}_{JII}	\bar{S}_{G}
0.5	2.1-2.7	1.7-2.7	121-204 (122)	69-175 (72)	5.0	4.9	3.1
	(2.1)	(1.8)					
2.0	2.0-2.7	1.7-2.7	118-205 (120)	68-176 (71)	5.9	5.7	4.0
	(2.0)	(1.7)					

^a Complete ranges (down to nucleation rates 1 nuclues.m⁻³.s⁻¹) with those calculated at corresponding average supersaturation ratios in parentheses (e.g., L_I = 2.1 nm at $\bar{S}_{\text{JI}} = 5.0$); note that the extreme values of $\Delta G_{\text{max,I}}$ and $\Delta G_{\text{max,II}}$ correspond to vanishingly small nucleation rates and thus, virtually no primary and secondary nucleation happens with barriers beyond ~ 170 and ~ 140 kJ.mol⁻¹, respectively.

S8. Mechanistic growth rate equations

There are a number of steps involved in the growth of solid particles the first being the diffusion of building units from the solution bulk to the surface of particles. A solid particle grows fastest when its faces are completely covered with kink sites. Under the above conditions, the particle growth is only limited by the diffusion of building blocks toward the particle surface. Therefore, diffusion-controlled growth theoretically dictates the highest growth rate a particle can achieve at a particular supersaturation.^{43,55} The mathematical expression for the maximum linear growth rate would then be

$$G_{\text{Diffusion}} = \frac{2k_A D}{3k_V \rho_{\text{solid}} L} c_{\text{eq}} (S - 1) \quad (\text{S39})$$

where L is the size of crystal, ρ_{solid} is the molar density of the precipitated solid, $c_{\text{eq}} = K_{\text{sp}}^{1/\nu}$ is the solubility of crystal ($\text{mol}\cdot\text{m}^{-3}$ solution), S is the supersaturation ratio, and D is the apparent diffusion of dissolved building units. This equation is simply Fick's first law for dilute solutions, correlating diffusive flux with concentration gradient, the latter approximated by relative supersaturation ratio ($S - 1$).²⁹

Crystal growth might be controlled by the integration of building units (monomers) onto the surface of particles if this step is much slower than the bulk diffusion process discussed earlier. Depending on the mechanism governing the attachment of building units to the surface of crystals, we typically encounter two types of integration-controlled growth equations. In this regard, integration could be controlled by screw dislocations present on the surface (BCF theory and its variations),⁵⁶ or it may be dominated by the role of two-dimensional surface nuclei. Even in a single system, however, under different conditions (e.g., supersaturation rise or depletion) there might be a transition from one mechanism to another with unknown borderline. To overcome this complication, a viable approach would be to define a growth rate analogous to that employed in diffusion-reaction theory (i.e., power law).^{43,55,57} The disadvantage of this approach, which is implemented in the PBE simulations performed here, is its semi-empirical nature.

Nielsen adapted the BCF theory to the growth of sparingly soluble electrolytes where the integration of cations into the kink sites from an electroneutral adsorption layer in equilibrium with solution is the rate-limiting step.^{58,59} Thus,

$$G_{\text{BCF}} = k_{\text{r,BCF}} \frac{(S-1)\sqrt{S} \times v \ln(S)}{1 + \frac{1}{\sqrt{3S}}} \quad (\text{S40})$$

where the growth rate constant reads

$$k_{\text{r,BCF}} = \frac{v_i K_{\text{ad}} c_{\text{eq}} k_{\text{B}} T v_0 N_{\text{A}}}{4\pi L_{\text{m}} \gamma_{\text{G}} \exp\left(\frac{\gamma_{\text{G}} L_{\text{m}}^2}{k_{\text{B}} T}\right)} \quad (\text{S41})$$

with the mole fraction-based rate constant (frequency) for the integration of building units (v_i ; s^{-1}) being related to the activation free energy ($\Delta G_{\text{i}}^{\#}$) of incorporation by means of the Eyring equation

$$v_i = \frac{k_{\text{B}} T}{h} \exp\left(-\frac{\Delta G_{\text{i}}^{\#}}{k_{\text{B}} T}\right) \quad (\text{S42})$$

In the equations above, K_{ad} is the adsorption equilibrium constant (30 for 2-1 and 1-2 electrolytes; 200 for 2-2 electrolytes),⁵⁹ $\gamma_{\text{G}} \equiv \min(\gamma_{\text{eff}}) = \gamma \left(\frac{a_{\text{r}}+1}{a_{\text{r}}+2}\right)$ is the effective interfacial tension for epitaxially incorporated monomers onto a substrate (i.e., attachment of building units to the substrate with perfect lattice match),^{46,51} v_0 is the molecular volume of water solvent ($3.00 \times 10^{-29} \text{ m}^3/\text{molecule H}_2\text{O}$), L_{m} is the size of building units (m), and h is the Planck's constant.

The other integration-controlled regime takes place when the formation of two-dimensional nuclei on the surface governs the growth of crystals. Depending on the assumptions made, particularly the relative rate of nuclei formation to their spreading, several equations have been derived in the literature. In this respect, if surface nuclei grow to form a complete new layer prior to the occurrence of the next nucleation event (the so-called mononuclear (MN) regime), the rate of crystal growth would be²⁹

$$G_{\text{MN}} = k_{\text{r,MN}} L^2 \exp\left(-\frac{\Delta G_{\text{max,s}}}{k_{\text{B}} T}\right) \quad (\text{S43})$$

where the activation free energy against two-dimensional surface nucleation is

$$\Delta G_{\max,s} = \frac{\beta' \Omega^{4/3} \gamma_G^2}{k_B T \times v \ln(S)} \quad (\text{S44})$$

with $\beta' = \frac{\beta_L^2}{4\beta_A}$ in which β_L and β_A are perimeter and area shape factors, respectively (e.g., $\beta_L = 4$ and $\beta_A = 1$ for a square surface nucleus). For a rectangular surface nucleus of arbitrary aspect ratio $a_{r,2D}$

$$\beta' = \frac{(a_{r,2D} + 1)^2}{a_{r,2D}} \quad (\text{S45})$$

On the other extreme, in polynuclear regime the spreading rate of surface nuclei is much smaller than their formation rate. In this case,^{29,59}

$$G_{PN} = k_{r,Exp} S^{7/6} (S - 1)^{2/3} (v \ln S)^{1/6} \exp\left(-\frac{\Delta G_{\max,s}}{3k_B T}\right) \quad (\text{S46})$$

Between these two extreme scenarios is the birth and spread (B&S) model where nuclei may be born on incomplete layers and spread at a constant rate, independent from each other.⁴³ In this case, the final growth rate expression reads⁶⁰

$$G_{B\&S} = k_{r,Exp} (S - 1)^{2/3} (v \ln S)^{1/6} \exp\left(-\frac{\Delta G_{\max,s}}{3k_B T}\right) \quad (\text{S47})$$

In the last two surface nucleation growth models the pre-exponential factor $k_{r,Exp}$ can be estimated as⁵⁹

$$k_{r,Exp} = 2L_m v_{in} \left(\frac{K_{ad} c_{eq}}{\rho_{Molar}}\right)^{4/3} \exp\left(-\frac{\gamma_G L_m^2}{k_B T}\right) \quad (\text{S48})$$

Over a limited range of supersaturation, the abovementioned growth rate expressions may be approximated by a power law form.²⁹ Therefore, the kinetic order of growth for mononuclear mechanism would be

$$g_{MN} = \frac{\beta' \Omega^{4/3} \gamma_G^2 (S - 1)}{(k_B T)^2 \times S \times v \ln^2(S)} \quad (\text{S49})$$

For polynuclear regime we have

$$g_{PN} = \frac{S - 1}{S} \left[\frac{7}{6} + \frac{2S}{3(S - 1)} + \frac{1}{6 \ln(S)} + \frac{\beta' \Omega^{4/3} \gamma_G^2}{3(k_B T)^2 \times v \ln^2(S)} \right] \quad (\text{S50})$$

and for B&S regime

$$g_{B\&S} = \frac{S-1}{S} \left[\frac{2S}{3(S-1)} + \frac{1}{6 \ln(S)} + \frac{\beta' \Omega^{\frac{4}{3}} \gamma_G^2}{3(k_B T)^2 \times v \ln^2(S)} \right] \quad (S51)$$

Inserting $\beta' = \pi$ (circular surface nuclei) and γ_G (31.84 and 33.48 mJ.m⁻² for 0.5 and 2 mL.min⁻¹, respectively) g values corresponding to various surface nucleation mechanisms can be obtained (Table S4) when S varies between its minimum and maximum value (1.022-5.06 and 1.017-5.97 for 0.5 and 2 mL.min⁻¹, respectively). It should be mentioned that the value of g ranges between 1 and 2 for BCF regime.²⁹

The value of exponent g roughly points toward the dominant integration mechanism at work. A value g = 1 indicates the dominance of rough surface growth (or dislocation-controlled growth at very high supersaturations) while g = 2 usually represents dislocation-controlled growth at relatively low supersaturations (parabolic law). Values g > 2, denoting stronger supersaturation dependence of growth rate, can arise under the dominance of surface nucleation mechanisms (mononuclear, polynuclear, or birth and spread growth mechanisms). Looking at Table S4 it is evident that PN mechanism cannot be responsible for the growth of C-S-H crystallites. Nevertheless, even though the fitted g values are closer to those corresponding BCF mechanism, MN and B&S mechanisms cannot be ruled out by this approach. Indeed, there might be parallel growth regimes at work during the precipitation process.

Table S5 summarizes the results of fitting power law growth rate output of PBE simulations by individual growth expressions (look at Fig. S3 for graphical representation). Also, Table 2 in the main text reports the results of regression with a compound B&S+BCF expression (look at Fig. 5 (c) in the main text, Fig. S7 (c), and Fig. S4 for the plots).

Table S4. Estimated kinetic order of growth corresponding to different surface nucleation models.

Q (mL.min ⁻¹)	Kinetic order of growth (g)
---------------------------	-----------------------------

	MN (Söhnel and Garside, 1992)	PN (Nielsen, 1984)	B&S (O'Hara and Reid, 1973)
0.5	1.02-151.6	2.0-51.4	1.1-51.4
2.0	0.96-216.9	2.1-73.2	1.1-73.1

Table S5. Results of fitting power law growth rate with individual surface integration-controlled models.

Q (mL.min ⁻¹)	Fit results	Growth rate equation		
		PN (Nielsen, 1984)	B&S (O'Hara and Reid, 1973)	BCF (Nielsen, 1981)
0.5	k _r	4.14×10 ⁻¹⁴	5.12×10 ⁻¹³	1.80×10 ⁻¹⁴
	β'	3.14	6.38	-
	Adjusted R ²	0.9945	0.9980	0.9970
	RMSE (m.s ⁻¹)	9.19×10 ⁻¹⁵	5.60×10 ⁻¹⁵	6.75×10 ⁻¹⁵
2.0	1 st parameter	3.73×10 ⁻¹⁴	5.41×10 ⁻¹³	1.53×10 ⁻¹⁴
	2 nd parameter	3.14	6.28	-
	Adjusted R ²	0.9972	0.9977	0.9988
	RMSE (m.s ⁻¹)	7.01×10 ⁻¹⁵	6.43×10 ⁻¹⁵	4.53×10 ⁻¹⁵

Fig. S5 shows the PBEM with a mononuclear growth expression fitted to experimental data (note that as mononuclear growth rate is size-dependent it shall not be fitted to the growth rate values of PBE simulations with size-independent power law expression). As it is obvious the regression is much inferior compared to that using a size-independent power law expression. This observation rules out the possibility of a mononuclear growth regime dominating the growth of C-S-H crystallites.

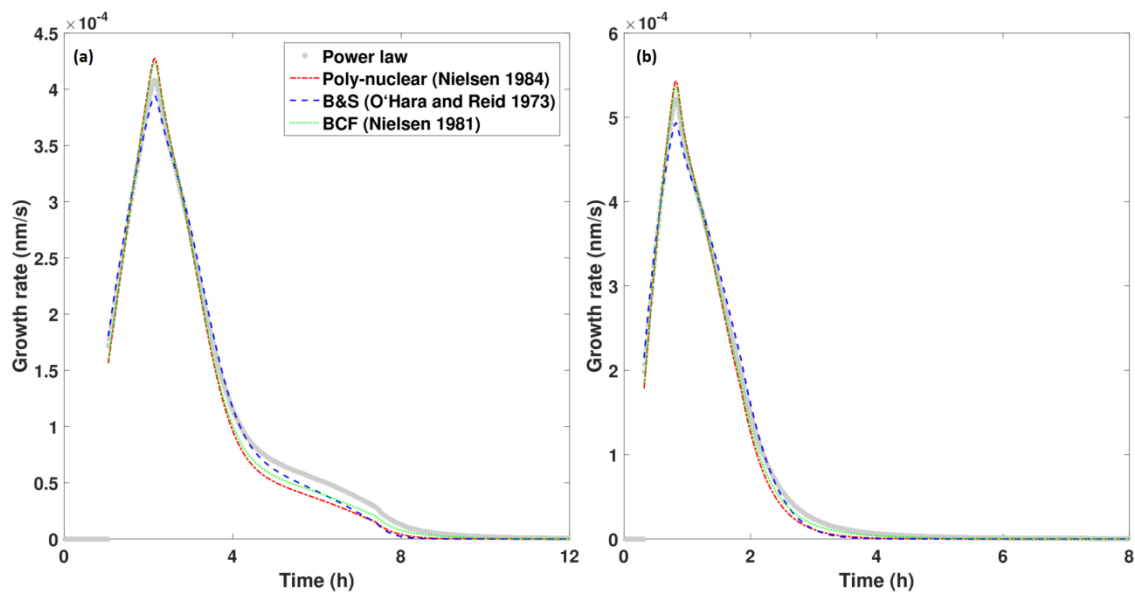


Fig. S3. Individual surface-controlled growth mechanisms fitted to power law data from PBEM for 0.5 (a) and 2.0 mL.min⁻¹ (b).

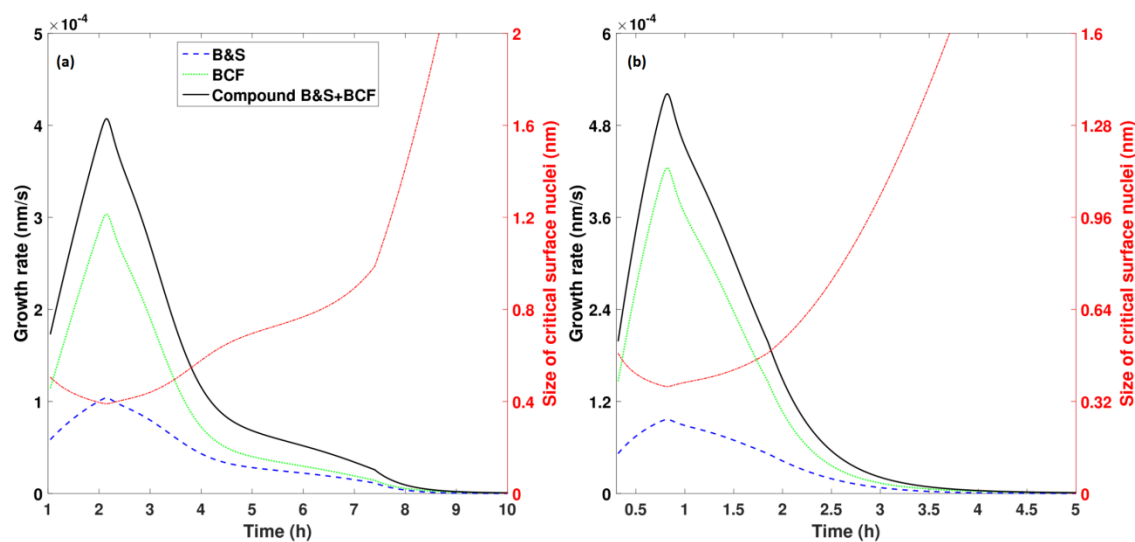


Fig. S4. Decomposition of compound B&S+BCF growth expression to its constituting parts along with the critical diameter of two-dimensional surface nuclei as a function of time for 0.5 (a) and 2.0 mL.min⁻¹ (b).

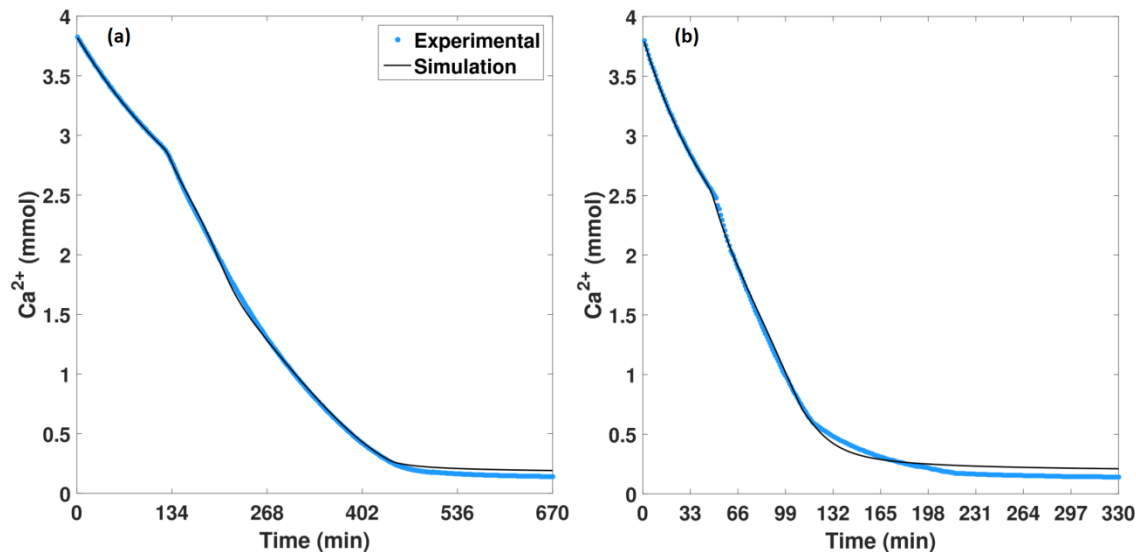


Fig. S5. PBE model with mononuclear growth expression fitted to experimental data at $Q = 0.5$ (a) and $2 \text{ mL}\cdot\text{min}^{-1}$ (b).

S9. Additional supplementary Fig.s

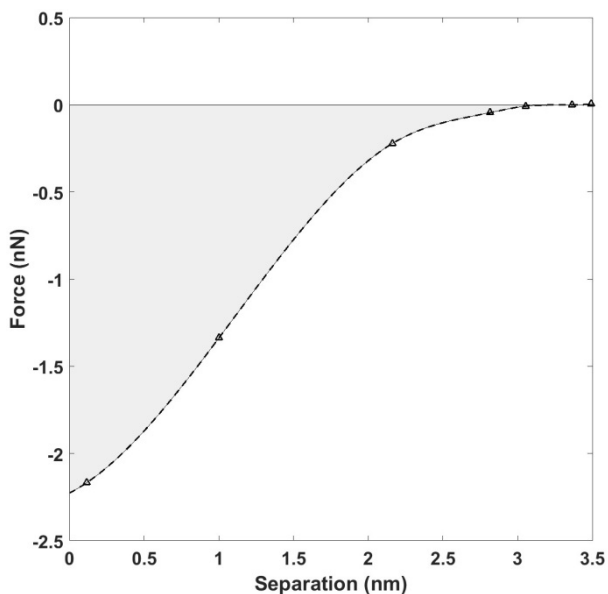


Fig. S6. Experimental (empty triangles) force data vs. separation for a flat C-S-H surface interacting with a C-S-H nanocrystal mounted on an AFM tip immersed in $\text{Ca}(\text{OH})_2$ solution with $\text{pH} = 12.5$ along with corresponding cubic spline interpolation (broken line) (reproduced from Fig. 7 in Ref. 61); the shaded area represents the integral work (= attractive energy) required to overcome the attraction between the two interacting bodies and pull them apart to a separation where there is a null force between them.

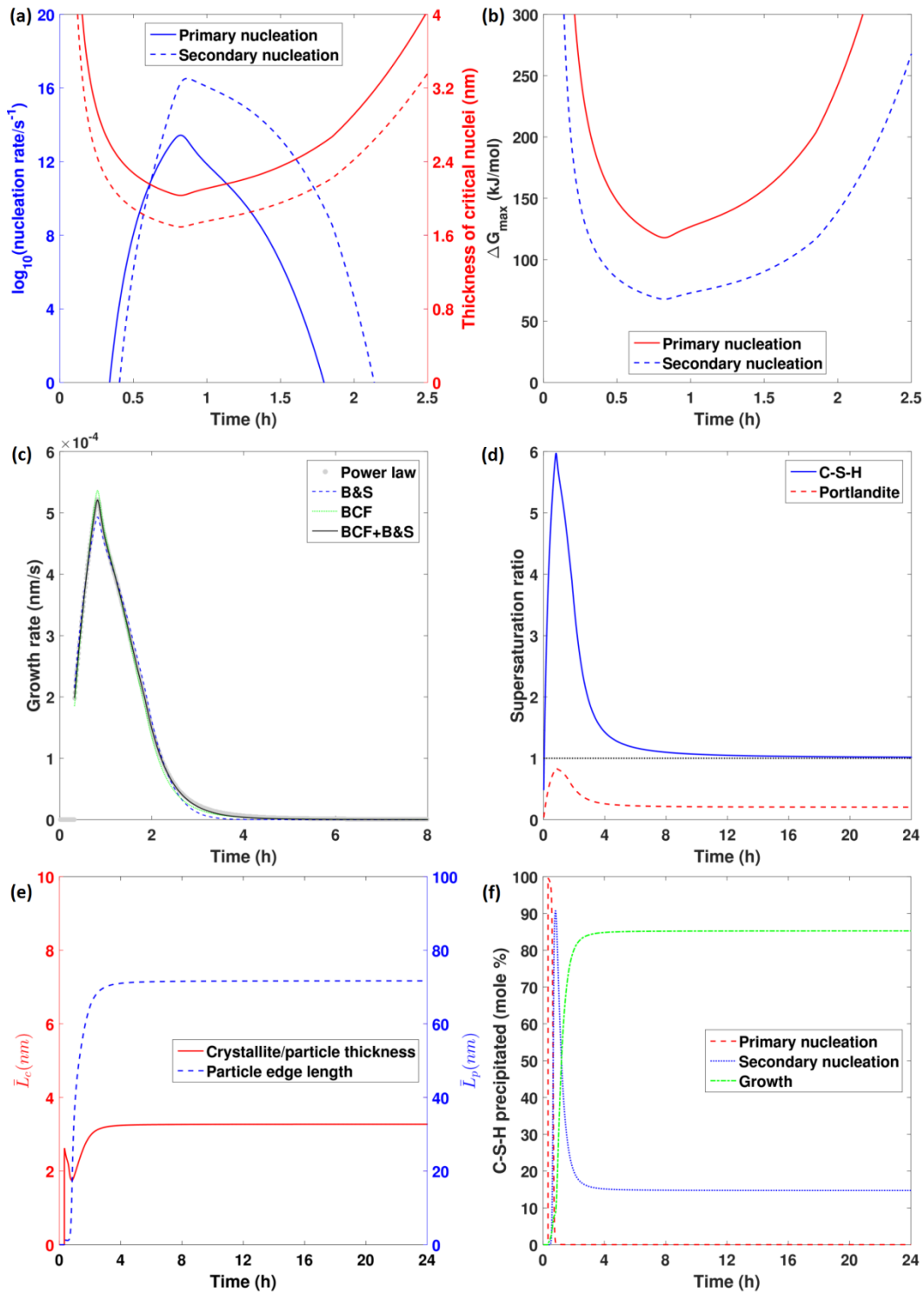


Fig. S7. Temporal PBE simulation outputs at $Q = 2.0 \text{ mL}\cdot\text{min}^{-1}$: (a) the rate of primary and secondary nucleation and the corresponding size of critical nuclei; (b) activation free energies against nucleation events; (c) C-S-H growth rate (power law) and its regression with different interface-controlled growth equations; (d) supersaturation ratio with respect to C-S-H and portlandite; (e) average C-S-H crystallite/particle thickness and its particle edge length; (f) cumulative contribution of various events to the overall amount of C-S-H precipitated.

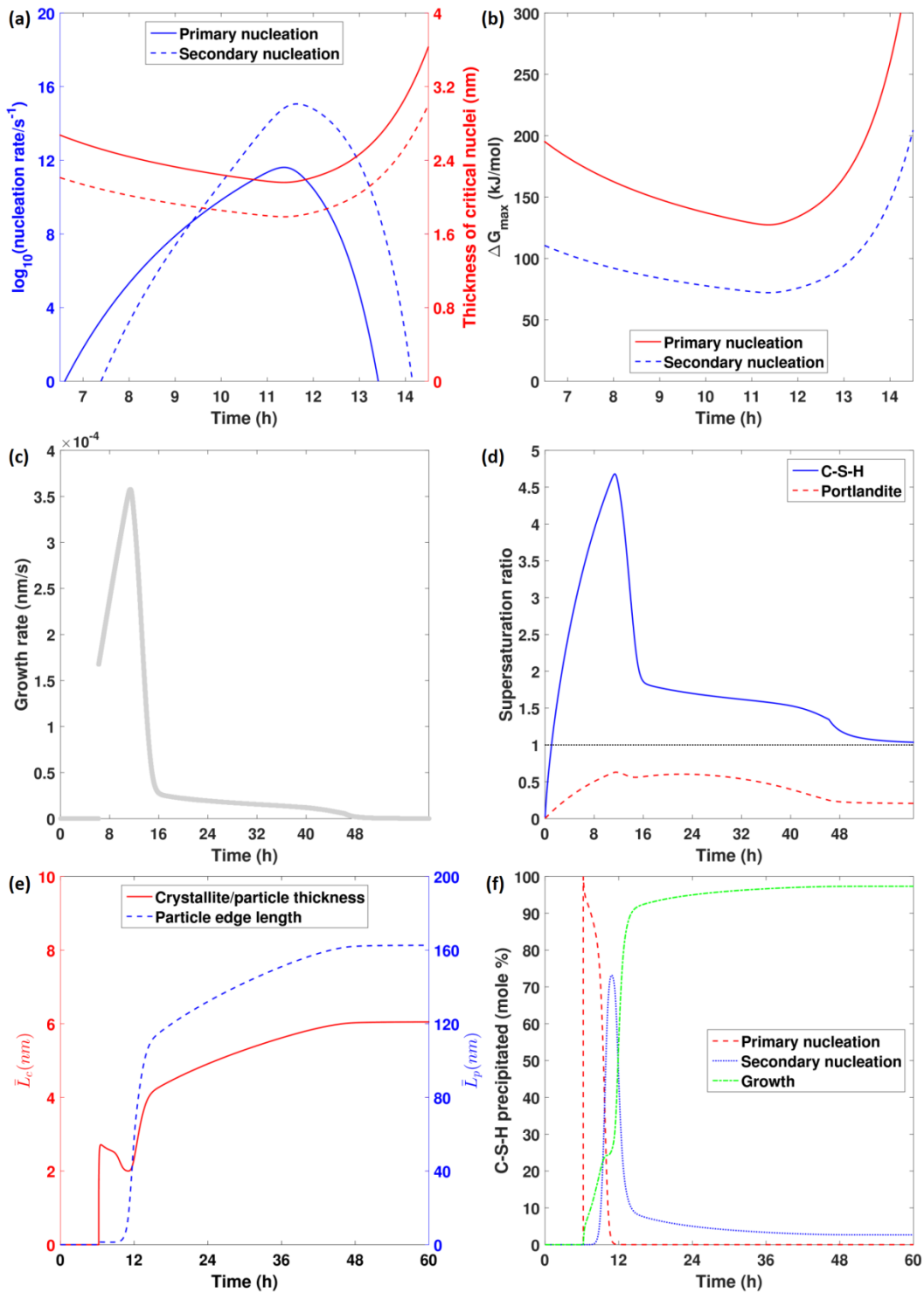


Fig. S8. Temporal PBE simulation outputs at $Q = 0.08 \text{ mL}\cdot\text{min}^{-1}$: (a) the rate of primary and secondary nucleation and the corresponding size of critical nuclei; (b) activation free energies against nucleation events; (c) C-S-H growth rate (power law); (d) supersaturation ratio with respect to C-S-H and portlandite; (e) average C-S-H crystallite/particle thickness and its particle edge length; (f) cumulative contribution of various events to the overall amount of C-S-H precipitated.

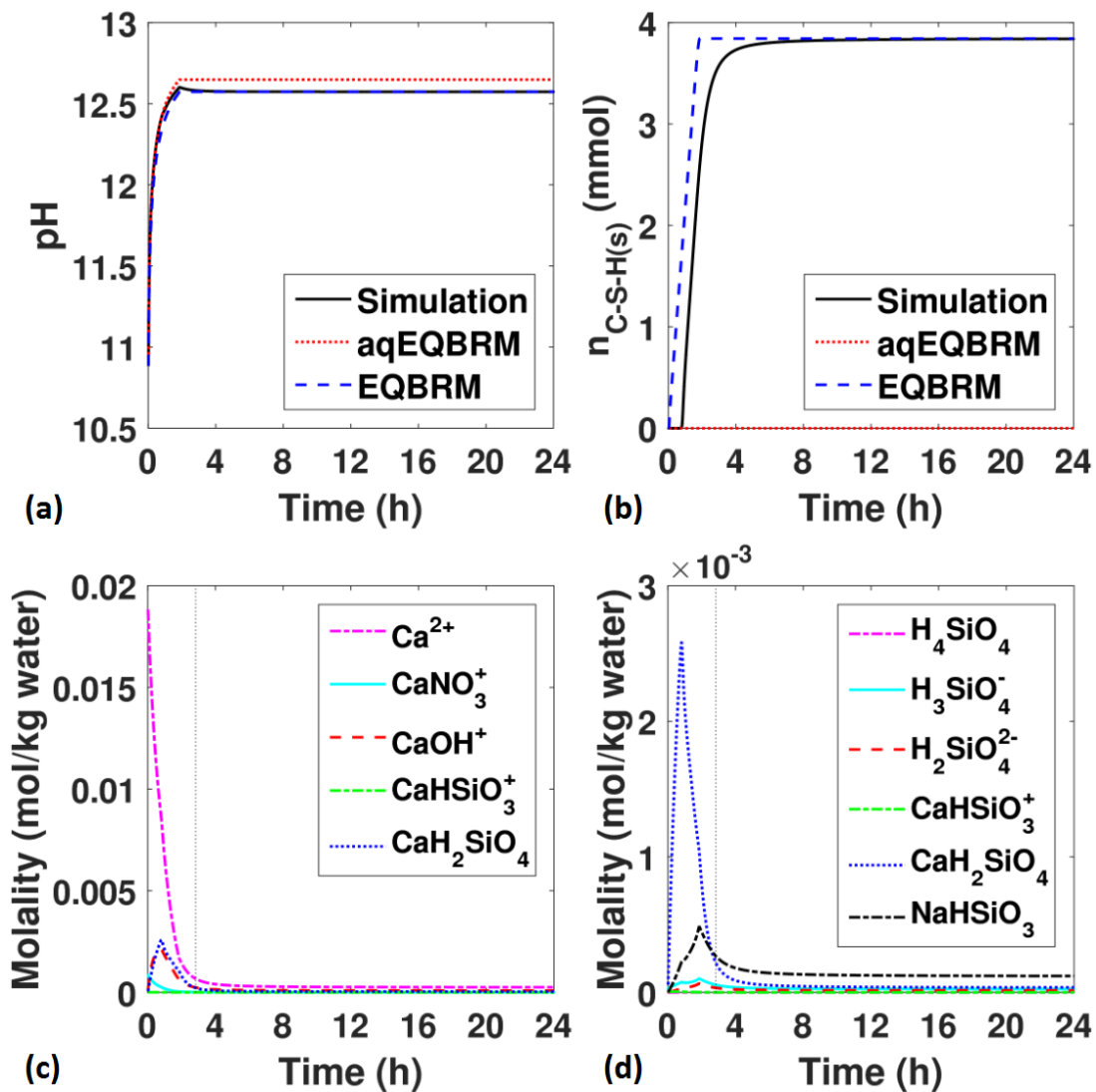


Fig. S9. Temporal kinetic speciation of C-S-H precipitation system ($Q = 2 \text{ mL}\cdot\text{min}^{-1}$): pH in the reaction medium (a), and the amount of solid C-S-H precipitating out of solution (b), along with the corresponding values predicted by equilibrium calculations including (EQBRM) and excluding (aqEQBRM) solid-liquid equilibrium; complete speciation of Ca- (c), and Si- (d) containing species present in aqueous solution (the dotted vertical line indicates the time at which the addition of Si solution stops).

S10. References

- (1) Kumar, A.; Walder, B. J.; Kunhi Mohamed, A.; Hofstetter, A.; Srinivasan, B.; Rossini, A. J.; Scrivener, K.; Emsley, L.; Bowen, P. *J. Phys. Chem. C* **2017**, 121 (32), 17188.

- (2) Hulburt, H. M.; Katz, S. *Chemical Engineering Science* **1964**, *19*, 555.
- (3) Randolph, A. D.; Larson, M. A. *Theory of Particulate Processes 2e: Analysis and Techniques of Continuous Crystallization*; Elsevier, 2012.
- (4) Marchisio, D. L.; Fox, R. O. *Computational models for polydisperse particulate and multiphase systems*; Cambridge University Press, 2013.
- (5) McGraw, R. *Aerosol Sci. Technol.* **1997**, *27*, 255.
- (6) Marchisio, D. L.; Piktorna, J. T.; Fox, R. O.; Vigil, R. D.; Barresi, A. A. *AIChE Journal* **2003**, *49*, 1266.
- (7) Gautschi, W. *Orthogonal polynomials: computation and approximation*; Oxford University Press on Demand, 2004.
- (8) Gordon, R. G. *J. Math. Phys.* **1968**, *9*, 655.
- (9) Sack, R.; Donovan, A. *Numerische Mathematik* **1971**, *18*, 465.
- (10) Wheeler, J. C. *Rocky Mountain J. Math.* **1974**, *4*, 287.
- (11) *OLI Studio*, version 9.2.4; OLI System, Inc.: Morris Plains, NJ, 2015; <http://www.olisystem.com/>.
- (12) Berner, U. *Radiochim. Acta.* **1988**, *44*, 387.
- (13) Berner, U. *Waste Manage.* **1992**, *12*, 201.
- (14) Kersten, M. *Environ. Sci. Technol.* **1996**, *30*, 2286.
- (15) Carey, J.; Lichtner, P. *Transport properties and concrete quality: Materials Science of Concrete* **2007**, *73*, 106.
- (16) Rahman, M. M.; Nagasaki, S.; Tanaka, S. *Cem. Concr. Res.* **1999**, *29*, 1091.
- (17) Kulik, D. A.; Kersten, M. *J. Am. Ceram. Soc.* **2001**, *84*, 3017.
- (18) Soler, J. M. *Thermodynamic description of the solubility of CSH gels in hydrated Portland cement*; Posiva Oy, 2007.
- (19) Prieto, M. *Rev. Mineral. Geochem.* **2009**, *70*, 47.

- (20) Prieto, M.; Heberling, F.; Rodríguez-Galán, R. M.; Brandt, F. *Prog. Cryst. Growth Charact. Mater.* **2016**, *62*, 29.
- (21) Thorstenson, D. C.; Plummer, L. N. *Am. J. Sci.* **1977**, *277*, 1203.
- (22) Prieto, M.; Putnis, A.; Fernández-Díaz, L.; López-Andrés, S. *J. Cryst. Growth* **1994**, *142*, 225.
- (23) Putnis, A.; Prieto, M.; Fernandez-Diaz, L. *Geol. Mag.* **1995**, *132*, 1.
- (24) Pina, C.; Putnis, A. *Geochim. Cosmochim. Acta* **2002**, *66*, 185.
- (25) Pina, C.; Putnis, A.; Astilleros, J. *Chem. Geol.* **2004**, *204*, 145.
- (26) Bullard, J. W.; Scherer, G. W. *J. Am. Ceram. Soc.* **2016**, *99*, 4137.
- (27) Lothenbach, B. *Mater. Struct.* **2010**, *43*, 1413.
- (28) Lothenbach, B.; Nonat, A. *Cem. Concr. Res.* **2015**, *78*, 57.
- (29) Söhnel, O.; Garside, J. *Precipitation: basic principles and industrial applications*; Butterworth-Heinemann, 1992.
- (30) Bandyopadhyaya, R.; Kumar, R.; Gandhi, K.; Ramkrishna, D. *Langmuir* **1997**, *13*, 3610.
- (31) VanBriesen, J. M.; Small, M.; Weber, C.; Wilson, J. *Modelling of Pollutants in Complex Environmental Systems* **2010**, *2*, 135.
- (32) Hanhoun, M.; Montastruc, L.; Azzaro-Pantel, C.; Biscans, B.; Frèche, M.; Pibouleau, L. *Chem. Eng. J.* **2013**, *215*, 903.
- (33) Galbraith, S.; Schneider, P. *Chem. Eng. J.* **2014**, *240*, 124.
- (34) Schroeder, B.; Harris, D.; Smith, S.; Lignell, D. *Cryst. Growth Des.* **2014**, *14*, 1756.
- (35) Zhu, Z.; Peng, Y.; Hatton, T. A.; Samrane, K.; Myerson, A. S.; Braatz, R. D. *Procedia Eng.* **2016**, *138*, 390.
- (36) Donnet, M.; Bowen, P.; Lemaitre, J. *J. Colloid Interface Sci.* **2009**, *340*, 218.
- (37) Rubin, J. *Water Resour. Res.* **1983**, *19*, 1231.
- (38) Kulik, D. A. *Cem. Concr. Res.* **2011**, *41*, 477.

- (39) Kulik, D. A.; Wagner, T.; Dmytrieva, S. V.; Kosakowski, G.; Hingerl, F. F.; Chudnenko, K. V.; Berner, U. R. *Computational Geosciences* **2013**, *17*, 1.
- (40) Crerar, D. A. *Geochim. Cosmochim. Acta* **1975**, *39*, 1375.
- (41) Anderson, G. M.; Crerar, D. A. *Thermodynamics in geochemistry: the equilibrium model*; Oxford University Press on Demand, 1993.
- (42) Parkhurst, D. L.; Appelo, C. **1999**.
- (43) Mersmann, A. *Crystallization technology handbook*; CRC Press, 2001.
- (44) Mersmann, A.; Bartosch, K. *J. Cryst. Growth* **1998**, *183*, 240.
- (45) Testino, A.; Buscaglia, M. T.; Buscaglia, V.; Viviani, M.; Bottino, C.; Nanni, P. *Chem. Mater.* **2004**, *16*, 1536.
- (46) Testino, A.; Buscaglia, V.; Buscaglia, M. T.; Viviani, M.; Nanni, P. *Chem. Mater.* **2005**, *17*, 5346.
- (47) Sounart, T. L.; Liu, J.; Voigt, J. A.; Hsu, J. W.; Spoerke, E. D.; Tian, Z.; Jiang, Y. *Adv. Funct. Mater.* **2006**, *16*, 335.
- (48) Sounart, T. L.; Liu, J.; Voigt, J. A.; Huo, M.; Spoerke, E. D.; McKenzie, B. *J. Am. Chem. Soc.* **2007**, *129*, 15786.
- (49) Liu, J.; Chen, X.; Wang, W.; Song, B.; Huang, Q. *Cryst. Growth Des.* **2009**, *9*, 1757.
- (50) Liu, J.; Cao, G.; Yang, Z.; Wang, D.; Dubois, D.; Zhou, X.; Graff, G. L.; Pederson, L. R.; Zhang, J. G. *ChemSusChem* **2008**, *1*, 676.
- (51) Marchisio, D. L. *Chem. Eng. Sci.* **2009**, *64*, 697.
- (52) Carino, A.; Testino, A.; Andalibi, M. R.; Pilger, F.; Bowen, P.; Ludwig, C. *Cryst. Growth Des.* **2017**.
- (53) Messac, A. *Optimization in Practice with MATLAB®: For Engineering Students and Professionals*; Cambridge University Press, 2015.

- (54) *MATLAB minimization algorithm "minimize"*, version 1.7, Oldenhuis, R., 2009;
<http://www.mathworks.com/matlabcentral/fileexchange/24298-minimize>.
- (55) Mullin, J. W. *Crystallization*; Butterworth-Heinemann, 2001.
- (56) Burton, W.-K.; Cabrera, N.; Frank, F. *Philos. Trans. R. Soc. London A Math. Phys. Eng. Sci.* **1951**, 243, 299.
- (57) Lewis, A.; Seckler, M.; Kramer, H.; Van Rosmalen, G. *Industrial Crystallization: Fundamentals and Applications*; Cambridge University Press, 2015.
- (58) Nielsen, A. *Pure Appl. Chem.* **1981**, 53, 2025.
- (59) Nielsen, A. E. *J. Cryst. Growth* **1984**, 67, 289.
- (60) Ohara, M.; Reid, R. C. *Modeling crystal growth rates from solution*; Prentice Hall, 1973.
- (61) Jönsson, B.; Wennerström, H.; Nonat, A.; Cabane, B. *Langmuir* **2004**, 20, 6702.